IOP Publishing Journal of Physics: Condensed Matter
J. Phys.: Condens. Matter **32** (2020) 175401 (8pp) https://doi.org/10.1088/1361-648X/ab680b

Effect of vacancy disorder in phase-change materials

Young-Sun Song and Seung-Hoon Jhi

Department of Physics, Pohang University of Science and Technology, Pohang 37673, Republic of Korea

E-mail: seunghoonjhi@gmail.com

Received 11 October 2019, revised 14 December 2019
Accepted for publication 6 January 2020
Published 28 January 2020

Abstract

Ge–Sb–Te-based phase-change materials (PCMs) exhibit contrasting electrical and optical properties upon change in atomic structures, which contain the octahedral *p*-orbital bonding and also substantial disordered vacancies. While extensive studies have been carried out, there is little detailed analysis of how the vacancy distribution and bonding nature are intercorrelated to affect the physical properties. We studied the effect of vacancy distribution on the octahedral *p*-bonding network in PCMs using a simple tight-binding model and *ab initio* calculations. We showed that the octahedral *p*-bonding network can be described as a collection of independent linear chains and that the vacancy disorders are rephrased as a distribution of atomic chain pieces. This finding enables to link the vacancy distribution to various aspects of materials properties such as total energy, structural distortions, and charge localization.

Keywords: phase-change materials, vacancy disorder, *p*-orbital bonding network

S Supplementary material for this article is available online

(Some figures may appear in colour only in the online journal)

1. Introduction

Chalcogenide-based phase-change materials (PCMs), primarily Ge–Sb–Te (GST) compounds, have been attracting great attraction for their fast structural transition between crystalline and amorphous phases [1–5]. As such, PCMs are promising candidate materials for the next-generation nonvolatile memory devices. Beside the fast transition, PCMs have many interesting properties such as topological insulators [6–8], thermoelectricity [9], and multiferroicity [10]. Also, PCMs were demonstrated to work as memristors, which are essential ingredients for neuromorphic devices that may realize device-level neural networks [11–13]. Rich physical interests and potential industrial applications are believed to stem from the structural peculiarity of PCMs, especially their unique bonding character [14, 15] and the vacancy disorders [16–21].

Octahedral-bonded cubic unit is considered to constitute an essential structural feature of PCMs. Such crystal-like structural motif also exists in amorphous phases and has been suggested to work as the nucleus that drives ultrafast crystallization [22, 23]. The octahedral symmetry and moderate difference in electronegativity between cation (4.6 eV for Ge, 4.85 eV for Sb) and anion (5.49 eV for Te) [24], as confirmed from the Bader charge analysis (the net charge of $+0.2|e|$ ~ $+0.5|e|$ for Ge and Sb and $-0.2|e|$ ~ $-0.4|e|$ for Te) [8], lead to the so-called 'octahedral *p*-orbital network (OPN)', a series of sequentially connected *p*-orbitals. An important consequence of the OPN is extraordinary long-ranged interactions, which cause the softening of optical modes and the large anharmonicity [25]. Disturbance in the OPN is responsible for the sharp contrast in optical and electrical properties between crystalline and amorphous phases of GST [26, 27]. Temperature-driven phonon instability in optical modes was found to be associated with the OPN as it disappears when the atoms form covalent bonding [28]. Distinguished from conventional covalent or resonant bonding, the OPN may be classified as 'metavalent bond' [29, 30].

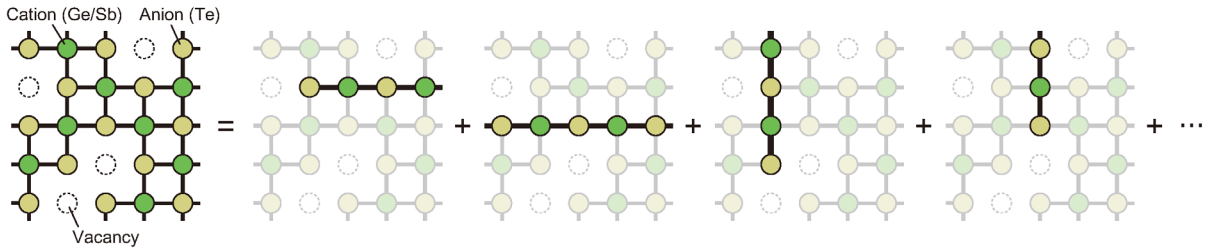

Figure 1. Schematic illustration of decomposing the OPN into linear chain pieces. The entire p-bonding network is represented as a collection of linear chain pieces along the three axes. Here, the 3D OPN system and its decomposition into linear chains are drawn in 2D for illustrative purpose (i.e. the chains directed normal to 2D plane are not shown). The cation, anion, and vacancy are represented as green, yellow balls, and white dotted circles, respectively.

One essential feature of the PCMs that governs the materials property is the significant amount of vacancies at the 4(b) (cation) sites. The structural stability [31], crystallization speed [32], band topology [33], and transport properties [34–37] of GST are found to be sensitive to the vacancy distribution. There have been several experimenal reports on the effect of cation and vacancy disorders in GST, in particular, associated with the metal-insulator transition [38] or structural transitions [39, 40]. A recent work in GeTe [41] also showed that the formation of Ge vacancies is crucial to the phase transition. Vacancy, being treated as defect, is considered at a level of local interaction while all the findings mentioned above indicate that vacancy may affect the electronic bonding at a more fundamental level. Systematic study on vacancy distribution and ordering in association with the bonding nature of GST is very desired.

In this paper, we studied the bonding nature of the OPN in GST and its change according to the vacancy distribution using the tight-binding method and *ab initio* calculations. We first analyzed the characteristics of the p-bonding network at the tight-binding level and converted the OPN into three independent linear chains within weak π-interaction approximation. We investigated the delocalization and inherent dynamic instability due to the long-ranged p-bonding in the linear chains. Next we studied the effect of the vacancy disorder as a disturbance to the long-ranged p-bonding network. In particular, we linked the vacancy ordering with the distribution in the length of chain pieces in the linear chains. We expressed various properties of the entire OPN such as structural, energetic, and transport properties, in terms of corresponding properties of individual linear chain pieces. We analyzed how these properties are affected as the vacancy disorder is changed.

2. General properties of OPN

2.1. Tight-binding model for OPN

We established a simple model to describe metastable GST, which has the cubic structure, in terms of the OPN. One feature in the bonding of GST is that s-orbitals of constituent elements are far separated from p-orbitals in energy and do not participate in the chemical bonding. The p-orbitals, on the other hand, dominate the states near the Fermi level in the cubic phase [25, 28, 42, 43]. Also the nearest–neighbor interaction is the most significant compared to other interactions between farther neighbors as supported by the *ab initio* tight-binding parameters from maximally localized Wannier functions calculations [44]. The first-nearest hopping parameters are about 10~50 times larger than the second-nearest ones (see table S1 in supplementary note 1 (stacks.iop.org/JPhysCM/32/175401/mmedia)). In this circumstance, the effective Hamiltonian for the bonding of cubic GST is described the best by the OPN, in which the interactions between p-orbitals along different axes are ignored. Now the p-orbital network is reduced to three independent chain networks along the cubic axes. We differentiate the atoms in anion (A) or cation (C) sites of NaCl cubic phase by the on-site energy $V_{\mathrm{A,C}}$ with $V_{\mathrm{C}} > V_{\mathrm{A}}$. In actual calculations, the on-site energy difference $V_{\mathrm{on}} = V_{\mathrm{C}} - V_{\mathrm{A}}$ is the independent parameter as the overall factor only shifts the Fermi energy. Furthermore, we treat the atomic species at anion (cation) sites as the same element A (C) unless specified since here our focus is on the vacancy configuration without exploring details arising from the difference in atomic species; i.e. Ge and Sb in GST are treated as the same element.

The tight-binding Hamiltonian for the OPN is constructed including only three types of interactions of σ-hopping integral V_σ, π-hopping integral V_π, and on-site energy difference V_{on} as following:

$$H = \sum_{\alpha} \left\{ \sum_{i\in\mathbb{C}} V_{\mathrm{on}} f^{\dagger}_{i\alpha} f_{i\alpha} + \sum_{i_\alpha || j_\alpha} V_\sigma \left(f^{\dagger}_{i\alpha} f_{j\alpha} + f^{\dagger}_{j\alpha} f_{i\alpha} \right) + \sum_{i_\alpha \perp j_\alpha} V_\pi \left(f^{\dagger}_{i\alpha} f_{j\alpha} + f^{\dagger}_{j\alpha} f_{i\alpha} \right) \right\}, \quad (1)$$

where $\alpha = (x, y, z)$ and $f_{i\alpha}$ is the electron operator at the ith atom's p_α-orbital. The summation $i \in \mathbb{C}$ runs over atoms at cation sites, and $i_\alpha || j_\alpha$ ($i_\alpha \perp j_\alpha$) indicates the summation for two nearest-neighboring atoms i, j connected parallel (perpendicular) to α-axis.

The σ-bonding is directional along the chain axis (the 1D linear p-chain), and the π-bonding represents the interaction

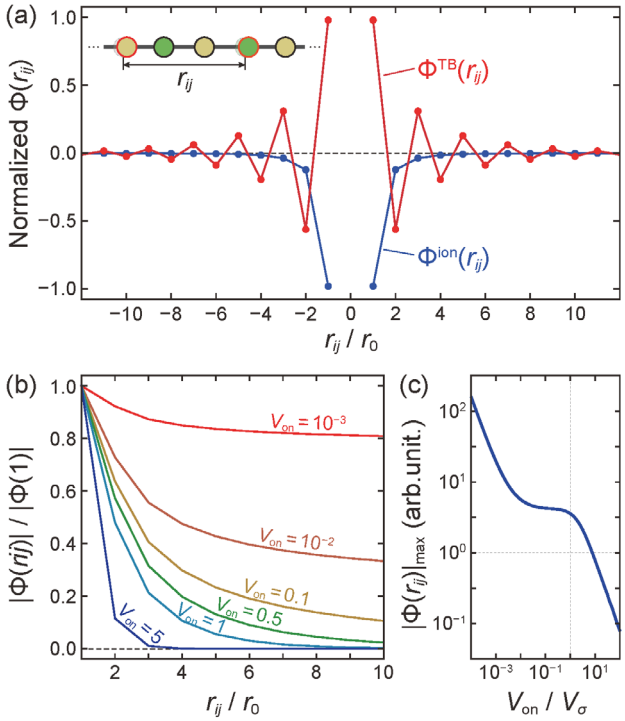

Figure 2. (a) Normalized IFCs from the tight-binding band energy term (Φ^{TB} (r_{ij}), red line) and ion–ion Coulomb repulsion term (Φ^{ion} (r_{ij}), blue line). (b) The absolute value of normalized Φ^{TB} for various V_{on}. (c) The maximum of absolute value Φ^{TB} as a function of V_{on}. Here we set $V_\sigma = 1$ for all cases.

between the adjacent 1D chains or the chain–chain interaction. Since the σ-bonding parameter V_σ is nearly 3–5 times larger than the π-bonding parameter V_π (table S1), the intra–chain coupling is more significant than the inter–chain interaction. Such large anisotropy among interactions is due to pronounced directionality of p-orbitals, allowing the bonding character of OPN to be described as a collection of all independent linear p-chains in the three axes. Within the approximation of neglecting π-interaction, one can express the total tight-binding energy as a sum of energies of each linear atomic chain as shown in figure 1 (see supplementary note 2). Individual chains now serve as a basic unit of OPN. Hereafter we do not consider π-interactions unless particularly mentioned.

2.2. Delocalized properties of OPN

Decomposition of the OPN into independent chains along three orthogonal directions simplifies the analysis of the physical properties of PCMs. In this section, we studied the interatomic force constants (IFCs) in the linear p-chain. The phonon softening is common in PCMs and the long-range IFCs are reported to be responsible for it [25, 28]. The behavior of IFCs thus hints at the formation of the OPN in PCMs. The IFC matrix in the 1D linear atomic chain can be represented as

$$\Phi_{ij} \equiv \frac{\partial^2 U}{\partial u_i \partial u_j} = \frac{\partial^2 E_{TB}}{\partial u_i \partial u_j} + \frac{\partial^2 V_{pair}}{\partial u_i \partial u_j}, \qquad (2)$$

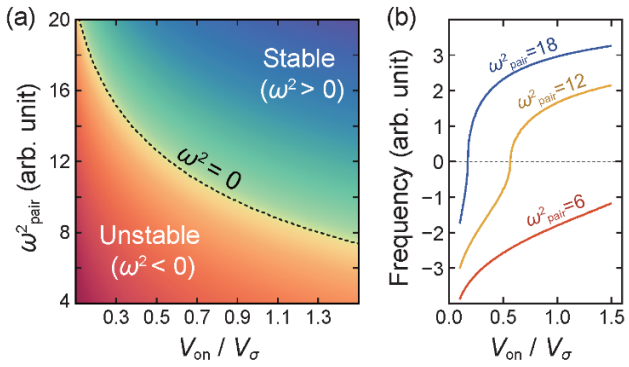

Figure 3. (a) LO mode frequency diagram for V_{on} and ω^2_{pair}. The stable region (positive frequency) is in blue and unstable region (negative frequency) in red, separated by black dashed. (b) LO mode frequency (in arbitrary unit) as a function of V_{on} for various values of ω^2_{pair}. Negative phonon frequency means the imaginary frequency ($\omega^2 < 0$).

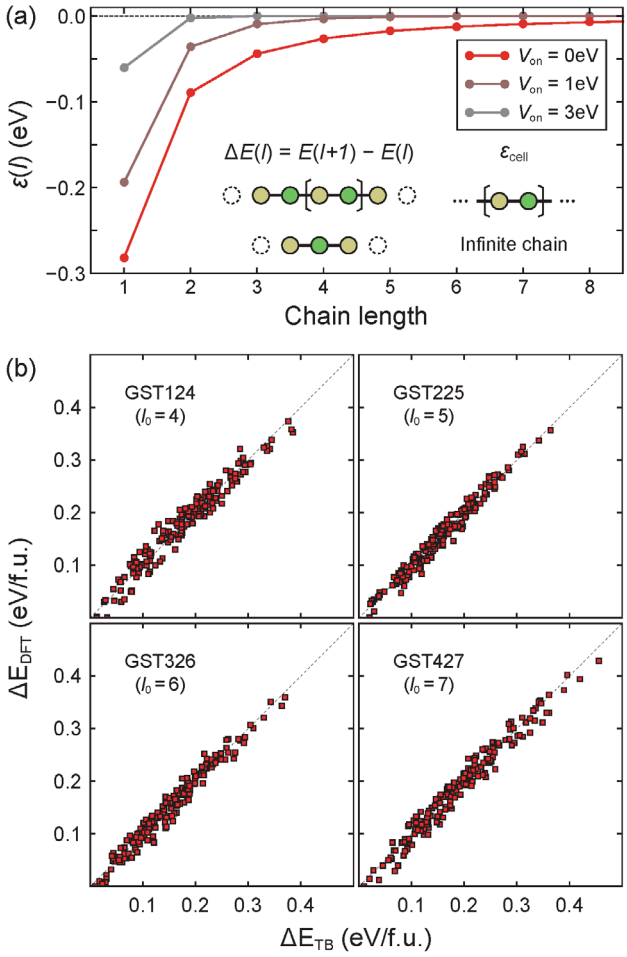

Figure 4. (a) The behavior of $\varepsilon(l)$ for three different values of V_{on}. Schematic descriptions for ΔE (l) and ε_{cell} are shown as the inset. (b) Calculated E_{TB} and E_{DFT} for 200 structures with different vacancy configurations of $Ge_1Sb_2Te_4$ (or GST124, hereafter the notation GSTxyz stands for $Ge_xSb_yTe_z$), GST225, GST326, and GST427. Both exhibit good correlation with correlation coefficient of 0.9771, 0.9874, 0.9841, and 0.9822, respectively. For all cases, $V_\sigma = 2.0$ eV, $V_\pi = -0.7$ eV, and $V_{on} = 1.5$ eV, and the scale factors for E_{TB} are rearranged to fit $E_{DFT}E_{DFT}$.

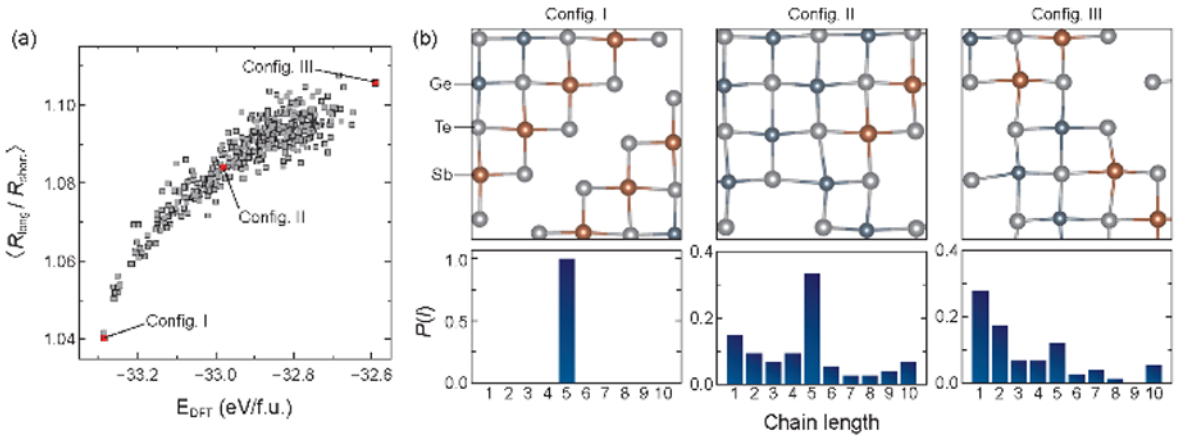

Figure 5. (a) The correlation between DFT total energy E_{DFT} and the long-short bond-length ratio averaged over all neighboring atomic pairs in the linear chains $\langle r_{\mathrm{long}}/r_{\mathrm{short}}\rangle$ for 400 different 4(b) site configurations. (b) The relaxed atomic structures and the chain length distribution function $P(l)$ of three exemplary configurations marked by red squares in (a).

where $u_i = r_i - r_{0,i}$ is the atomic displacement of the ith atom. Here the total energy U is represented as a sum of the tight-binding band energy E_{TB} and pair potential V_{pair} [45]. Figure 2(a) shows the IFCs from the tight-binding energy, $\Phi_{ij}^{\mathrm{TB}} = \Phi^{\mathrm{TB}}(r_{ij})$, as a function of $r_{ij} = r_j - r_i$. The wave-packet-shaped Φ^{TB} is widely spread over the 1D linear chain. Comparing the IFC with that from the ion–ion Coulomb repulsion, $\Phi^{\mathrm{ion}}(r_{ij}) = \frac{\partial^2 V_{\mathrm{ion}}}{\partial u_i \partial u_j} \sim -r_{ij}^{-3}$, with $V^{\mathrm{ion}}(r_{ij}) \sim r_{ij}^{-1}$ (blue line in figure 2(a)), we found that the IFCs from the tight-binding band energy extend in distance more than those from the pair potential term that decays much faster than V^{ion}. This finding indicates that the long-range behavior of IFCs is a direct consequence of the bonding characteristic of the OPN.

Figures 2(b) and (c) show $\left|\Phi^{\mathrm{TB}}(r_{ij})\right|$ with the tight-binding parameters. It tends to decrease fast with V_{on}, which indicates that Φ^{TB} is very short-ranged. In our tight-binding model, the on-site energy difference may correspond to the electronegativity difference between the anion and cation. Relative strength between V_{on} and V_σ primarily determines the bonding character. For $V_{\mathrm{on}} || V_\sigma$, we have the ionic bonding character without long-ranged interactions, consistent with the DFT calculations [25]. The other limiting case of $V_{\mathrm{on}} \to 0$ corresponds to the p-bonding network, and Φ^{TB} becomes now fully delocalized with its amplitude diverging. Typical OPN systems including GST compounds have $V_{\mathrm{on}}/V_\sigma = 10^{-2} \sim 10^{0}$, retaining delocalization properties moderately without experiencing divergence in the potential. (See Supplementary note 3 for more detailed mathematical description on the tight-binding IFCs.)

Another noticeable feature of Φ^{TB} is the alternate sign with increasing r_{ij} while Φ^{ion} decays monotonically. The alternation in sign of Φ^{TB} determines the stability of longitudinal optical (LO) modes at Γ point in the 1D chain. The long-range feature and the sign change in Φ^{TB} affect the LO mode the most among all modes in the 1D chain [25].

The LO mode frequency is determined from the combination of Φ^{TB} and Φ^{pair}, i.e. the competition between relative strength of the long-ranged p-bonding andthe short-ranged repulsive potential (supplementary note 4). Figure 3 shows the LO-mode frequency as a function of V_{on}/V_σ and ω_{pair}^2, the pair-potential contribution to the frequency. We observe that extended p-bonding chains (or small V_{on}/V_σ) destabilize the LO mode. Since the band gap is associated with reduction in Φ^{TB} (see supplementary note 3), the band gap opening by dimerization (or increase in V_{on}) can relieve the instability. This is basically equivalent to the Peierls instability that the gap opening induced by dimerization stabilizes the electronic band energy [46]. Inclusion of weak π-interaction does not significantly affect the delocalized nature of IFCs associated with the long-ranged interactions. We note that other network systems with different bonding geometry like graphene do not exhibit extended feature in IFCs (see supplementary note 5).

3. Role of vacancy distribution

3.1. Vacancy distribution and geometry of OPN

A vacancy at a 4(b) site splits a single chain into two pieces, disturbing the OPN. In our σ-interaction-only-approximation, each piece of linear chains is energetically independent of each other (see supplementary note 2). In this scheme, we analyzed the whole system by investigating the behavior of individual chain pieces and summing up their properties. Now the vacancy configuration in the OPN determines the chain-length distribution $P(l)$ with average chain length $l_0 = 1/\nu$, ν the vacancy density. For vacancies fully ordered in single layers, $P(l) = \delta_{l,l_0}$, whereas fully disordered vacancies give $P(l) = \nu(1-\nu)^{l-1}$, a form of geometric distribution. The distribution function $P(l)$ represents the entire system as a collection of individual chain pieces. The whole system is readily understood in terms of the vacancy distribution once the length-dependent behavior of physical properties of linear chain pieces is analyzed. Next, we focus on the length dependence of the tight-binding energy, phonon instability, and the charge localization of linear chain pieces.

3.2. Total energy and vacancy distribution

The tight-binding energy of a single chain piece in the OPN should depend only on the chain length l, given as

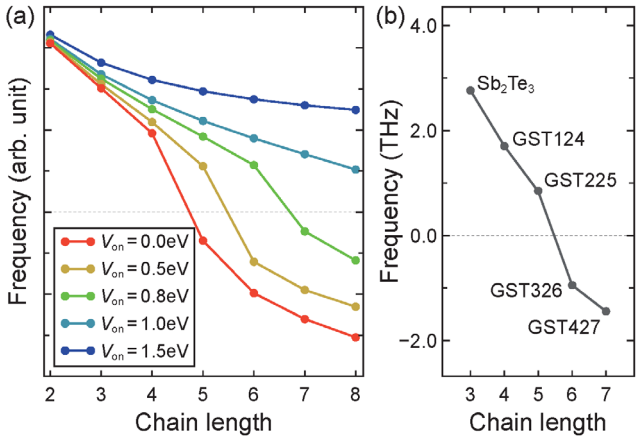

Figure 6. (a) Estimated frequency of the LO mode as a function of the chain length with various values of V_{on}. (b) The frequency of an optical mode at Γ point (or the E_u mode) of hexagonal GST compounds as a function of the averaged chain length based on DFT calculations. The chain length $l = 3$–7 correspond to different compositions of Sb_2Te_3, GST124, GST225, GST326, and GST427, respectively.

$E(l)$. We define the offset energy $\varepsilon(l) \equiv \Delta E(l) - \varepsilon_{cell}$, where $\Delta E(l) = E(l+1) - E(l)$ and ε_{cell} is the energy of a unit cell in the infinitely-long chain. The offset energy $\varepsilon(l)$ may measure the closeness of a chain piece of length l to the infinite chain. Figure 4(a) shows the behavior of $\varepsilon(l)$ with V_{on}. We find that $\varepsilon(l)$ converges relatively slowly for small V_{on}, where the energy gain from an additional unit depends on the chain length. In this regime, the total energy of the system depends sensitively on the vacancy distribution. On the other hand, for large V_{on}, $\varepsilon(l)$ converges fast to zero, indicating that the effect of finite length in chain energy is significant only near the vacancy sites.

Since the offset energy $\varepsilon(l) < 0$ for all l (see figure 4(a)), we can show that short chains have larger energy than long chains (supplementary note 6). The total tight-binding energy, $E_{TB} = \sum_l P(l) E(l)$, thus has bigger contribution from short chains than long chains, reflecting the degree of the vacancy disorder through $P(l)$. As the vacancy is disordered, the portion of short chains is increased and so is E_{TB}. For a given vacancy density, E_{TB} is thus the minimum at the fully ordered vacancies. (See supplementary note 5 for detailed mathematics of the tight-binding energy and the chain-length distribution.)

Figure 4(b) shows E_{TB} and E_{DFT} (the DFT total energy) for various vacancy configurations of GST compounds with different vacancy densities, which show good correlation. In DFT calculations, Ge and Sb are treated within the virtual crystal approximation. Our simplified tight-binding energy reproduces reasonably well the DFT total energies and enables qualitative and quantitative analysis of vacancy disorders in GST compounds.

In the hexagonal GST compounds, the adjacent Te–Te layers are coupled by the van der Waals (vdW) interaction, which may affect the physical properties such as the emergence of the gapless Weyl node [47, 48]. While the metastable cubic phase does not contain such ordered vacancy layers, we investigated possible effect of vdW interaction near vacancies. We used the DFT-D2 method by Grimme [49] to find the total energy reduced by about 0.15 eV per formula unit and the volume contraction of about ~7% in metastable GST. The average Te-vacancy-Te distance is decreased by ~5%, indicating that the volume contraction is mostly due to the Te-vacancy-Te reduction. We found that the effect of the vdW interaction is slightly enhanced as the vacancy is ordered.

3.3. Dynamic stability controlled by vacancy distribution

The chain length determines the decay length of Φ^{TB} and thus the frequency of the LO mode. As the chain length is increased, Φ^{TB} approaches quickly to that of infinitely-long chains, attaining the inherent instability of the 1D infinite chain. Figure 5(a) shows the drastic softening in the LO mode as the chain length is increased, especially for small V_{on}. DFT calculations also supports the length-dependent LO instability in the OPN. Figure 5(b) shows the softening of the optical phonon mode at the Γ point in the hexagonal GST compounds with different composition ratio [28]. We note that large V_{on} weakens the length dependence of Φ^{TB}, similar to the case of E_{TB}.

The softening of the LO mode results in the Peierls-type dimerization in the linear chains. Disordered vacancy produces broad spreading in the chain-length distribution for a given vacancy density, containing long chains that inherently possess the LO instability. The Peierls-type dimerization by the LO instability and the subsequent structural distortions may occur easily for disordered vacancy configurations. We verified this relation from DFT calculations of GST225 structures with 400 different vacancy configurations. To measure the degree of dimerization, we calculated the ratio in length of long and short bonds $\langle r_{long}/r_{short} \rangle$ averaged over all neighboring atomic pairs [28]. Figure 6(a) shows that $\langle r_{long}/r_{short} \rangle$ scales roughly linear with E_{DFT}, confirming that the vacancy disorder increases both the structural distortion and the total energy of the OPN. Figure 6(b) shows a specific example of atomic distortions for three different vacancy distributions, which highlights drastic atomic distortions for disordered vacancies.

Atomic misalignments induced by the distortions destroy the long-range nature of the OPN from increased *s*-*p* orbital mixing [28]. We also studied the effect of atomic misalignments on the conductivity and optical dielectric constant (see supplementary note 7). The change in bonding characteristics from atomic distortion is supported by a recent study that found gradual transition in the bonding nature of PCM from delocalized *p*-bonds to localized covalent bonds due to the Peierls distortion [29]. Our study suggests that the OPN in PCMs can be manipulated by tuning the vacancy disorders.

3.4. Charge localization by vacancy distribution

Another important effect of vacancy is to cause the charge localization. Zhang *et al*, found that the metal–insulator

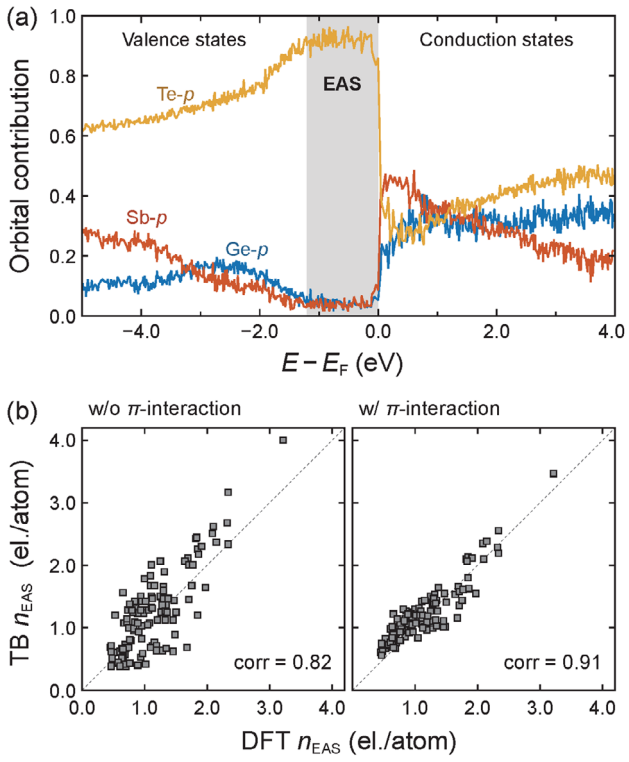

Figure 7. (a) The projection of the states near the Fermi level (E_F) to p-orbitals of Te (yellow), Sb (red), and Ge (blue). The energy range for the EASs is marked as the shaded region. (b) Comparison of tight-binding and DFT calculations of the amplitude of the EAS at each Te atom for a chosen GST225 structure with disordered vacancies. The tight-binding calculation with the π-interaction gives better match with DFT results (the right panel, correlation coefficient of 0.91) than the one without it (the left panel, correlation coefficient of 0.82).

transition in GST is driven by the charge localization near the vacancy sites due to unpaired p-electrons of adjacent Te atoms [35]. Here we give an alternative explanation for the charge localization in a framework of the linear chain pieces.

We first investigated the eigenstates of the OPN. In a linear chain piece, the highest occupied molecular orbital (HOMO) is a linear combination of p-orbitals at A-sites only without mixing of p-orbitals at B-sites. Here we call this state as 'exclusive A-state (EAS)'. DFT calculations also show that Te p-orbitals contribute almost exclusively to the states near the Fermi level, confirming these states to be the EASs in our chain model (see figure 7(a)). The EASs should be responsible for the transport properties of the OPN (see supplementary note 8). In a linear chain piece, the EAS is equally spread over the Te atoms and the amplitude of the EAS at each Te atom scales with the inverse of the chain length. For the OPN, the amplitude of the EAS is given as the harmonic mean of the chain lengths along all axes, indicating that the EAS tend to be more populated at short-length chains.

Disordered vacancies produce a wide spread in chain length and subsequent localization of the EAS at short-length chains. The vacancies thus directly affect the electrical conductivity through variation in p-network geometry. The chain-piecewise charge localization illustrates the 1D-like character embedded in the strongly directional OPNs.

The population of the EAS derived in the tight-binding model is confirmed by the DFT calculations. We can easily show that it is given as $\sum_\alpha l_\alpha^{-1}$ ($\alpha = x, y, z$) in the tight-binding model. Figure 7(b) shows the squared amplitude (n_{EAS}) calculated in one of 400 GST225 structures with disordered vacancy (see supplementary note 8 for details). We calculated n_{EAS} for each Te atom by projecting all the states lying in the energy range of the EASs into Te p-orbitals. For total 125 Te atoms, we found the correlation coefficient of 0.82 between the two methods. Inclusion of the π-bonding interaction improves the correlation, as it reflects the diffusion of the EAS due to the chain–chain interactions. Our calculations indicate that the EAS is primarily spread over linear chain pieces rather than being simply localized near the vacancy sites. In other words, electrons in EASs are more likely localized in Te atoms neighboring vacancies than in saturated Te atoms since Te atoms in short chains have bigger chances of being neighbors to the vacancy sites.

We note that the energy levels in our model inherit intrinsic inaccuracy, not to mention the well-known band-gap underestimation in DFT calculations (0.43 eV in average compared to experimental value of 0.5 eV). In addition, the tight-binding model in this work does not consider the site-dependent variation in the onsite energy in disordered vacancies. The vacancy-induced variation in the onsite energy and the absence of Coulomb potential at the vacancy sites will split the degenerate levels of EASs to increase the Fermi level. This means that the vacancy distribution directly affects the electronic transport properties by modulating the localized nature of EASs (see supplementary note 8 for the absence of degeneracy by the onsite energy variation).

4. Conclusion

We studied the octahedral p-bonding network and the effect of the vacancy ordering in PCMs adopting the linear chain model. We found the delocalization and inherent dynamic instability in the OPN due to long-ranged IFC in the linear chains. The strong directionality of p-orbitals in the OPNs enables the decomposition of the 3D network into linear chain pieces at the tight-binding level. The inherent instability of the OPN may help explain the atomic distortion associated with the phase change in PCMs. We showed that the vacancy disorder in the OPN can be rephrased as the distribution of the chain length and that the physical property of the entire OPN is also described by corresponding terms of individual chain pieces that exhibit a simple length-dependence. The total energy, charge localization, bond distortion, electrical conductivity, and optical dielectric constant of OPN were analyzed as the vacancy disorder was changed. Our results give an insight on a fundamental connection between the vacancies and the material properties

in terms of *p*-orbital bonding network, which will help improve device performance by adjusting the vacancy disorder quantitatively.

Acknowledgments

This study was supported by the National Research Foundation of Korea (NRF) grant (No. 2018R1A2B6003492 and No.2018R1A5A6075964) funded by the Korea government (MSIT). Supercomputing resources including technical support was provided by Supercomputing Center, Korea Institute of Science and Technology Information (Contract No. KSC-2013-C3-042).

ORCID iDs

Seung-Hoon Jhi https://orcid.org/0000-0003-4623-2950

References

[1] Ovshinsky S R 1968 Reversible electrical switching phenomena in disordered structures *Phys. Rev. Lett.* **21** 1450
[2] Lankhorst M H, Ketelaars B W and Wolters R 2005 Low-cost and nanoscale non-volatile memory concept for future silicon chips *Nat. Mater.* **4** 347–52
[3] Wełnic W, Pamungkas A, Detemple R, Steimer C, Blügel S and Wuttig M 2006 Unravelling the interplay of local structure and physical properties in phase-change materials *Nat. Mater.* **5** 56–62
[4] Wuttig M and Yamada N 2007 Phase-change materials for rewriteable data storage *Nat. Mater.* **6** 824–32
[5] Lencer D, Salinga M, Grabowski B, Hickel T, Neugebauer J and Wuttig M 2008 A map for phase-change materials *Nat. Mater.* **7** 972–77
[6] Kim J, Kim J and Jhi S-H 2010 Prediction of topological insulating behavior in crystalline Ge–Sb–Te *Phys. Rev.* B **82** 201312
[7] Kim J, Kim J, Kim K-S and Jhi S-H 2012 Topological phase transition in the interaction of surface dirac fermions in heterostructures *Phys. Rev. Lett.* **109** 146601
[8] Sa B, Zhou J, Sun Z, Tominaga J and Ahuja R 2012 Topological insulating in GeTe/Sb_2Te_3 phase-change superlattice *Phys. Rev. Lett.* **109** 096802
[9] Lee J, Asheghi M and Goodson K E 2012 Impact of thermoelectric phenomena on phase-change memory performance metrics and scaling *Nanotechnology* **23** 205201
[10] Tominaga J *et al* 2015 Giant multiferroic effects in topological GeTe-Sb2Te3 superlattices *Sci. Technol. Adv. Mater.* **16** 014402
[11] Kuzum D, Jeyasingh R G, Lee B and Wong H-S P 2011 Nanoelectronic programmable synapses based on phase change materials for brain-inspired computing *Nano Lett.* **12** 2179–86
[12] Burr G W *et al* 2015 Experimental demonstration and tolerancing of a large-scale neural network (165 000 synapses) using phase-change memory as the synaptic weight element *IEEE Trans. Electron Devices* **62** 3498–507
[13] Tuma T, Pantazi A, Le Gallo M, Sebastian A and Eleftheriou E 2016 Stochastic phase-change neurons *Nat. Nanotechnol.* **11** 693
[14] Kolobov A V, Fons P, Frenkel A I, Ankudinov A L, Tominaga J and Uruga T 2004 Understanding the phase-change mechanism of rewritable optical media *Nat. Mater.* **3** 703–8
[15] Shportko K, Kremers S, Woda M, Lencer D, Robertson J and Wuttig M 2008 Resonant bonding in crystalline phase-change materials *Nat. Mater.* **7** 653–58
[16] Nonaka T, Ohbayashi G, Toriumi Y, Mori Y and Hashimoto H 2000 Crystal structure of GeTe and $Ge_2Sb_2Te_5$ meta-stable phase *Thin Solid Films* **370** 258–61
[17] Matsunaga T and Yamada N 2002 A study of highly symmetrical crystal structures, commonly seen in high-speed phase-change materials, using synchrotron radiation *Japan. J. Appl. Phys.* **41** 1674
[18] Eom J-H, Yoon Y-G, Park C, Lee H, Im J, Suh D-S, Noh J-S, Khang Y and Ihm J 2006 Global and local structures of the Ge–Sb–Te ternary alloy system for a phase-change memory device *Phys. Rev.* B **73** 214202
[19] Sun Z, Zhou J and Ahuja R 2006 Structure of phase change materials for data storage *Phys. Rev. Lett.* **96** 055507
[20] Da Silva J L, Walsh A and Lee H 2008 Insights into the structure of the stable and metastable (GeTe) m (Sb_2Te_3) n compounds *Phys. Rev.* B **78** 224111
[21] Lotnyk A, Bernütz S, Sun X, Ross U, Ehrhardt M and Rauschenbach B 2016 Real-space imaging of atomic arrangement and vacancy layers ordering in laser crystallised $Ge_2Sb_2Te_5$ phase change thin films *Acta Mater.* **105** 1–8
[22] Kalikka J, Akola J, Larrucea J and Jones R 2012 Nucleus-driven crystallization of amorphous $Ge_2Sb_2Te_5$: a density functional study *Phys. Rev.* B **86** 144113
[23] Rao F *et al* 2017 Reducing the stochasticity of crystal nucleation to enable subnanosecond memory writing *Science* **358** 1423–7
[24] Pearson R G 1988 Absolute electronegativity and hardness: application to inorganic chemistry *Inorg. Chem.* **27** 734–40
[25] Lee S, Esfarjani K, Luo T, Zhou J, Tian Z and Chen G 2014 Resonant bonding leads to low lattice thermal conductivity *Nat. Commun.* **5** 3525
[26] Huang B and Robertson J 2010 Bonding origin of optical contrast in phase-change memory materials *Phys. Rev.* B **81** 081204
[27] Kolobov A, Krbal M, Fons P, Tominaga J and Uruga T 2011 Distortion-triggered loss of long-range order in solids with bonding energy hierarchy *Nat. Chem.* **3** 311–6
[28] Song Y-S, Kim J and Jhi S-H 2018 Phonon instability and broken long-ranged p bond in Ge–Sb–Te phase-change materials from first principles *Phys. Rev. Appl.* **9** 054044
[29] Wuttig M, Deringer V L, Gonze X, Bichara C and Raty J-Y 2018 Incipient metals: functional materials with a unique bonding mechanism *Adv. Mater.* **30** 1803777
[30] Zhu M, Cojocaru-Mirédin O, Mio A M, Keutgen J, Küpers M, Yu Y, Cho J Y, Dronskowski R and Wuttig M 2018 Unique bond breaking in crystalline phase change materials and the quest for metavalent bonding *Adv. Mater.* **30** 1706735
[31] Wuttig M, Lüsebrink D, Wamwangi D, Wełnic W, Gilleßen M and Dronskowski R 2007 The role of vacancies and local distortions in the design of new phase-change materials *Nat. Mater.* **6** 122

[32] Lee T and Elliott S 2011 Structural role of vacancies in the phase transition of $Ge_2Sb_2Te_5$ memory materials *Phys. Rev.* B **84** 094124
[33] Kim J and Jhi S-H 2015 Disorder-induced structural transitions in topological insulating Ge–Sb–Te compounds *J. Appl. Phys.* **117** 195701
[34] Siegrist T, Jost P, Volker H, Woda M, Merkelbach P, Schlockermann C and Wuttig M 2011 Disorder-induced localization in crystalline phase-change materials *Nat. Mater.* **10** 202–8
[35] Zhang W, Thiess A, Zalden P, Zeller R, Dederichs P, Raty J-Y, Wuttig M, Blügel S and Mazzarello R 2012 Role of vacancies in metal–insulator transitions of crystalline phase-change materials *Nat. Mater.* **11** 952–6
[36] Jost P *et al* 2015 Disorder-induced localization in crystalline pseudo-binary GeTe–Sb_2Te_3 alloys between $Ge_3Sb_2Te_6$ and GeTe *Adv. Funct. Mater.* **25** 6399–406
[37] Zhang W, Wuttig M and Mazzarello R 2015 Effects of stoichiometry on the transport properties of crystalline phase-change materials *Sci. Rep.* **5** 13496
[38] Zhang B *et al* 2016 Element-resolved atomic structure imaging of rocksalt $Ge_2Sb_2Te_5$ phase-change material *Appl. Phys. Lett.* **108** 191902
[39] Zhu M, Ren K, Liu L, Lv S, Miao X, Xu M and Song Z 2019 Direct observation of partial disorder and zipperlike transition in crystalline phase change materials *Phys. Rev. Mater.* **3** 033603
[40] Lotnyk A, Dankwort T, Hilmi I, Kienle L and Rauschenbach B 2019 *In situ* observations of the reversible vacancy ordering process in van der Waals-bonded Ge–Sb–Te thin films and GeTe–Sb_2Te_3 superlattices *Nanoscale* **11** 10838–45
[41] Sist M, Kasai H, Hedegaard E M and Iversen B B 2018 Role of vacancies in the high-temperature pseudodisplacive phase transition in GeTe *Phys. Rev.* B **97** 094116
[42] Cohen M H, Falicov L M and Golin S 1964 Crystal chemistry and band structures of the group V semimetals and the IV–VI semiconductors *IBM J. Res. Dev.* **8** 215–27
[43] Albanesi E A, Okoye C, Rodriguez C, y Blanca E P and Petukhov A 2000 Electronic structure, structural properties, and dielectric functions of IV–VI semiconductors: PbSe and PbTe *Phys. Rev.* B **61** 16589
[44] Mostofi A A, Yates J R, Lee Y-S, Souza I, Vanderbilt D and Marzari N 2008 wannier90: A tool for obtaining maximally-localised Wannier functions *Comput. Phys. Commun.* **178** 685–99
[45] Sigalas M and Papaconstantopoulos D 1994 Transferable total-energy parametrizations for metals: applications to elastic-constant determination *Phys. Rev.* B **49** 1574
[46] Gaspard J-P and Ceolin R 1992 Hume-Rothery rule in V–VI compounds *Solid State Commun.* **84** 839–42
[47] Sa B, Miao N, Zhou J, Sun Z and Ahuja R 2010 *Ab initio* study of the structure and chemical bonding of stable $Ge_3Sb_2Te_6$ *Phys. Chem. Chem. Phys.* **12** 1585–8
[48] Kim J, Kim J, Song Y-S, Wu R, Jhi S-H and Kioussis N 2017 Weyl node assisted conductivity switch in interfacial phase-change memory with van der Waals interfaces *Phys. Rev.* B **96** 235304
[49] Grimme S 2006 Semiempirical GGA-type density functional constructed with a long-range dispersion correction *J. Comput. Chem.* **27** 1787–99